

MAGI: A New High-Performance Airborne Thermal-Infrared Imaging Spectrometer for Earth Science Applications

Jeffrey L. Hall, Richard H. Boucher, Kerry N. Buckland, David J. Gutierrez, John A. Hackwell, B. Robert Johnson, Eric R. Keim, Nery M. Moreno, Michael S. Ramsey, Mazaher G. Sivjee, David M. Tratt, *Senior Member, IEEE*, David W. Warren, and Stephen J. Young

Abstract—A new airborne facility instrument for Earth science applications is introduced. The Mineral and Gas Identifier (MAGI) is a wide-swath (programmable up to $\pm 42^\circ$ off nadir) moderate spectral resolution thermal-infrared (TIR) imaging spectrometer that spans the 7.1- to 12.7- μm spectral window in 32 uniform and contiguous channels. Its spectral resolution enables improved discrimination of rock and mineral types, greatly expanded gas-detection capability, and generally more accurate land-surface temperature retrievals. The instrument design arose from trade studies between spectral resolution, spectral range, and instrument sensitivity and has now been validated by flight data acquired with the completed sensor. It offers a potential prototype for future space-based TIR instruments, which will require much higher spectral resolution than is currently available in order to address more detailed climate, anthropogenic, and solid Earth science questions.

Index Terms—Dyson spectrometer, imaging spectrometer, remote sensing, thermal infrared (TIR).

I. INTRODUCTION

WE INTRODUCE an advanced high radiometric sensitivity, moderate spectral resolution, airborne thermal-infrared (TIR) imaging spectrometer for Earth science. The Mineral and Gas Identifier (MAGI) spans the 7.1- to 12.7- μm spectral region in 32 uniform contiguous channels and was conceived as both a fundamental science tool and a test bed

Manuscript received November 6, 2014; revised February 11, 2015; accepted March 18, 2015. The MAGI sensor was developed with support from the NASA Instrument Incubator Program (IIP), funded by the NASA Earth Science Technology Office. All trademarks, service marks, and trade names are the properties of their respective owners; their appearance does not imply endorsement by The Aerospace Corporation or NASA. The work of M. S. Ramsey was supported in part by the IIP program and the ASTER Science Team. IIP support also supported completion of an M.S. graduate degree at the University of Pittsburgh.

J. L. Hall, R. H. Boucher, K. N. Buckland, D. J. Gutierrez, J. A. Hackwell, E. R. Keim, N. M. Moreno, M. G. Sivjee, D. M. Tratt, D. W. Warren, and S. J. Young are with The Aerospace Corporation, Los Angeles, CA 90009-2957 USA (e-mail: jeffrey.l.hall@aero.org; richard.h.boucher@aero.org; kerry.n.buckland@aero.org; david.j.gutierrez@aero.org; john.a.hackwell@aero.org; eric.r.keim@aero.org; nery.m.moreno@aero.org; mazaher.g.sivjee@aero.org; David.M.Tratt@aero.org; david.w.warren@aero.org; stephen.j.young@aero.org).

B. R. Johnson, deceased, was with The Aerospace Corporation, Los Angeles, CA 90009-2957 USA.

M. S. Ramsey is with the Department of Geology and Planetary Science, University of Pittsburgh, Pittsburgh, PA 15260-3332 USA (e-mail: mramsey@pitt.edu).

Color versions of one or more of the figures in this paper are available online at <http://ieeexplore.ieee.org>.

Digital Object Identifier 10.1109/TGRS.2015.2422817

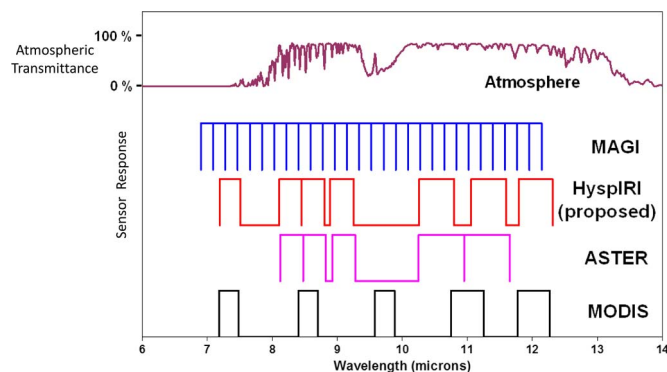


Fig. 1. MAGI wavelength bands compared with those of current Earth-orbiting TIR imagers and the proposed HypsIRI-TIR sensor.

for validation of future space-based TIR imager concepts. In particular, MAGI was designed to emulate and test sensor configurations and measurement scenarios that were envisioned to evolve for the Hyperspectral Infrared Imager (HypsIRI) mission [1], [2].

TIR data from orbit have a long history in many Earth science applications such as the monitoring and characterization of incipient and active volcanic eruptions [3]–[5], drought susceptibility in critical agricultural and ecological regions [6]–[8], and multiscale environmental impacts of urbanization and land-use change [9], [10], among other topics. Over the past several decades, high spatial resolution Earth-orbiting imaging sensors have only offered between one and five channels, and therefore, the TIR spectral region has been primarily used for measuring surface temperatures rather than detailed compositional analysis of solid surfaces or gases. Traditionally, the visible/near-infrared and short-wave infrared (SWIR) regions have been used to remotely map certain lithologies of the Earth's surface, particularly those of clay and carbonate mineralogy. However, the TIR spectral region offers the unique ability to distinguish between most silicate, carbonate, and sulfate minerals and many gases, which has been demonstrated with some success using the five-band Advanced Spaceborne Thermal Emission and Reflection Radiometer (ASTER [11]) TIR products [12]–[14]. Furthermore, high spectral resolution TIR sensors have been successfully used on planetary missions to detect numerous minerals and surficial units [15], [16]. The MAGI sensor will therefore greatly improve the ability to discriminate silicate minerals, as well as other major rock-forming

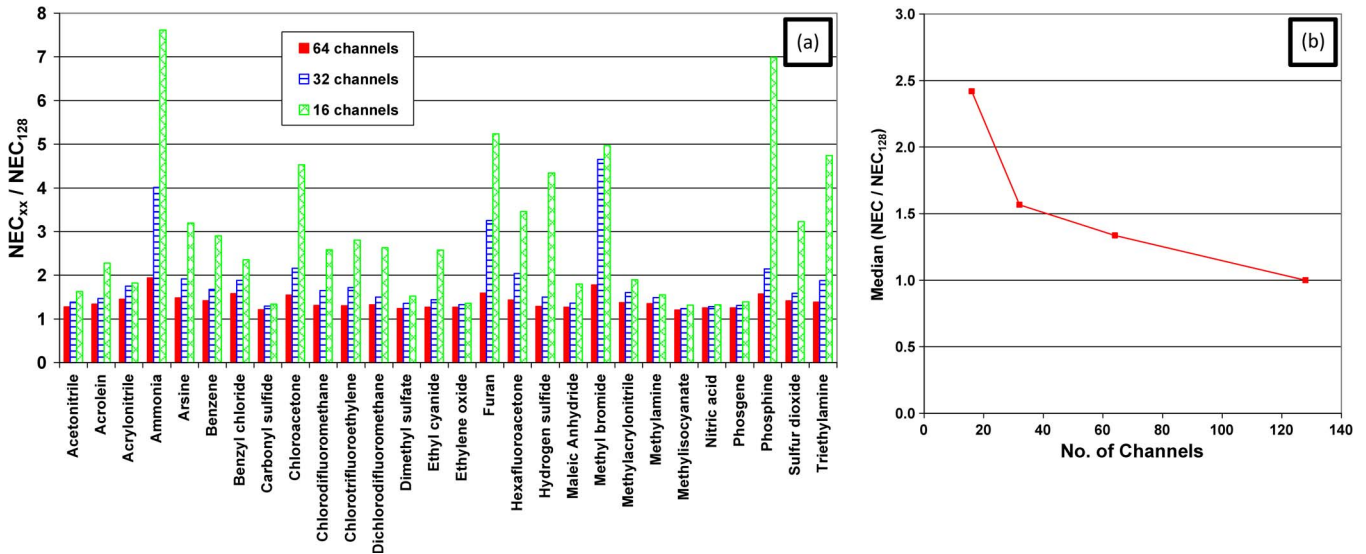


Fig. 2. (a) Values of the NEC (see text for definition) for 64, 32, and 16 wavelength channels for 28 of 56 chemicals, ratioed to the values for 128 bands. Larger ratios imply a less capable instrument. For most gases, the sensitivity loss from 128 to 32 channels is less than a factor of 2. (b) Median NEC ratio versus number of channels (all chemicals). A significant penalty is incurred in reducing from 32 to 16 channels [34].

minerals (e.g., carbonates, sulfates, and phosphates), and IR-active gas species at a spectral resolution that balances accurate detection against data volume.

A TIR imaging spectrometer with the spectral resolution of MAGI enables improvements in retrieved surface spectral emissivity and in-scene atmospheric compensation (ISAC) techniques that permit more accurate temperature retrievals [17]. Fig. 1 illustrates the wavelengths of the contiguous MAGI bands in comparison with current Earth-orbiting TIR imagers and the proposed HypSIRI-TIR sensor. For example, accurate surface temperature estimation is important for studies of heat flux for evapotranspiration, assessing vulnerability to drought, and estimating soil moisture using thermal inertia [6], [18], [19]. In so doing, MAGI will contribute to a more complete understanding of local-to-regional scale surface energy balance in areas of changing land-cover and land-use patterns such as agricultural areas at desert margins and regions undergoing persistent deforestation or urbanization. These phenomena have a significant impact on the water, carbon, and climate cycles on multiple scales, and their accurate characterization is key to the formulation of robust policy and strategies for monitoring, predicting, and mitigating the effects of climate change.

II. PARAMETRIC TRADE ANALYSES

The MAGI sensor design conceptualization was originally supported by a series of trade analyses between spectral resolution, wavelength limits, sensor noise, and spatial resolution. These studies used archival data that were collected with the Spatially Enhanced Broadband Array Spectrograph System (SEBASS) sensor [20].

A. Gas Detection

The trade between gas detection sensitivity and spectral resolution was accomplished against a list of 56 gases found in the

environment, either as anthropogenic pollutants or from natural sources such as volcanoes. The matched filter gas detection approach used has been previously described [21], [22].

Noise-equivalent contrast (NEC) was used as a measure of relative sensitivity. Contrast is the product of the gas column density and the temperature difference between the gas and the underlying scene. The NEC was determined using a 128-spectral-channel SEBASS scene known from previous analysis to contain no gas plumes. Data sets were created with 64, 32, and 16 equivalent spectral channels with noise added to simulate the levels expected for MAGI. Library reference spectra were taken from existing sources [23]–[25]. Fig. 2 displays the ratio of the computed NECs to the 128-channel NEC data set for 28 of the 56 gases, and it also provides a summary plot of the median NEC ratio for all gases. Species that have narrow diagnostic spectral features (for example, ammonia, hydrogen sulfide, and methyl bromide) suffer the greatest sensitivity loss from reduced spectral resolution, and this performance penalty is markedly worse for resolutions coarser than 32 channels. The NEC ratios of only 4 of the 56 gases were significantly worsened if the long-wavelength cutoff was moved from 13.1 to 12 μm , whereas additional 2 gases become very difficult to detect for an 11.5- μm cutoff.

This study concluded that a 32-channel instrument would have a sensitivity penalty of $\sim 60\%$ relative to 128 channels. Furthermore, approximately 90% of the gases examined were detectable with a 12- μm long-wavelength cutoff.

B. Mineral Identification

The mineral mapping study used data collected by SEBASS over Cuprite, NV, in October 2002. The Cuprite site has been extensively used for sensor testing of mineral and rock discrimination [26]–[28] because of its geological diversity and terrain that is unobscured by vegetation. The data were processed to remove atmospheric absorption and emission features using the

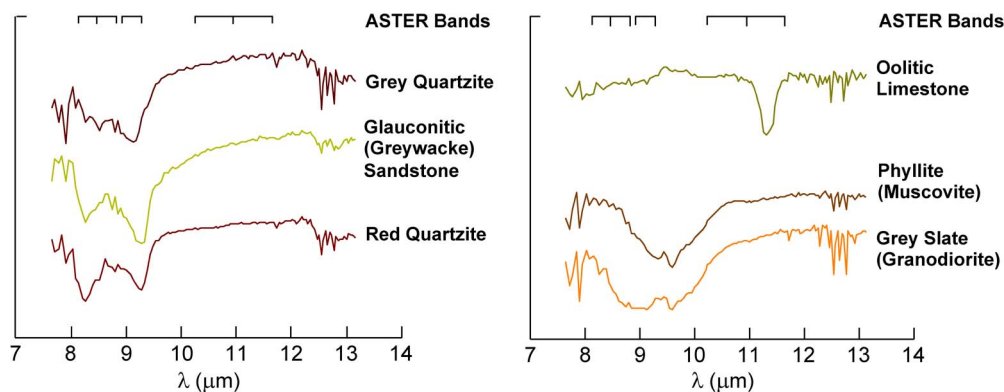


Fig. 3. Six of the primary endmembers from the 128-channel SEBASS data for the Cuprite, Nevada data set. Their identification with minerals/rocks from the ASTER spectral library, based on spectral shape, is noted. Identifications noted in parentheses are close, but second best, fits [34].

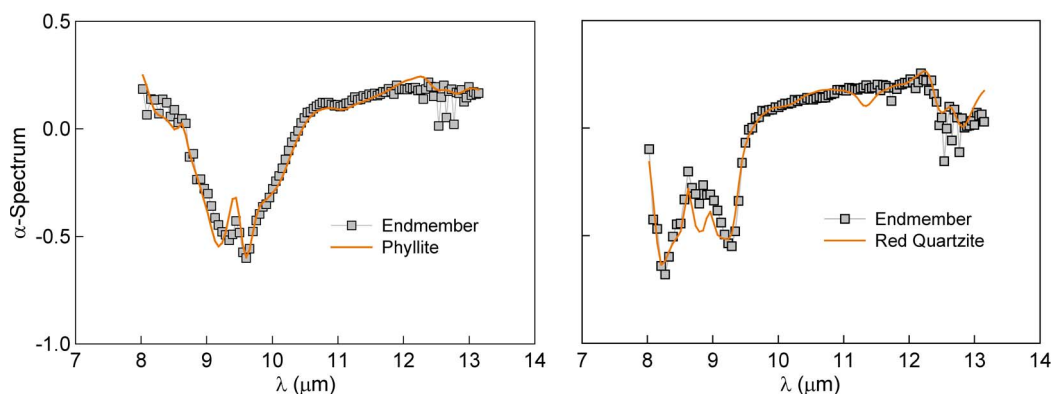


Fig. 4. Fits of two endmember spectra to entries in the ASTER spectral library [34].

ISAC algorithm [29] and converted from radiance to emissivity. Endmember spectra were extracted from the emissivity imagery using the simplex inflation method [30]. Six of these endmembers displaying wide spatial distribution were used in the study and are shown in Fig. 3.

The material type corresponding to each of these endmembers was identified by comparison to spectra in the ASTER spectral database (<http://speclib.jpl.nasa.gov>). Example fits between two extracted endmembers and ASTER library spectra are shown in Fig. 4. A constrained least square regression was used to determine the endmember composition of each pixel in the eight data sets. The constraint was imposed that all endmembers be detected with positive fraction. The regression procedure gives the fractional composition for each endmember for every pixel; however, for this paper, only the dominant endmember was mapped. Fig. 5 shows the dominant endmember spatial distributions for various degrees of spectral degradation. The 32-band image shown is visually identical to the original 128-band image. In contrast, some confusion begins to occur with respect to identification among the silicate endmembers where the resolution is reduced to 16 spectral channels. The degradation to the five ASTER channels results in still further loss of identification fidelity. Note, however, that the loss of fidelity at the ASTER level is not nearly as severe as that which occurs in the gas detection study described previously.

A visual comparison of these results with SWIR results obtained with the ASTER sensor [31] suggests broad agreement,

although no detailed comparison of our mineral identification and distribution results with other remote sensing or *in situ* measurements has been carried out for this paper.

The conclusion of this analysis is consistent with that made by the Mars exploration teams for the miniature thermal emission spectrometer (TES) sensor on Mars Exploration Rovers and the TES spectrometer in orbit on the Mars Global Surveyor spacecraft for deciphering the mineralogy/lithology of Mars. Both of these instruments have ~ 45 channels in the 7.8- to 12.0- μm wavelength range [32], [33].

III. SENSOR DESIGN

The conceptual design of MAGI was informed by the parametric trade analyses described above, focusing on the optimum TIR spectral resolution for achieving a majority of the science objectives of TIR imaging sensors [34]. As we have seen, the outcome of this exercise was a 32-channel TIR design point that is intermediate between that of coarse-resolution multispectral airborne TIR imagers (e.g., MASTER [35] and eMAS [36]) and the “hyperspectral” TIR imager family, such as the legacy SEBASS [20] instrument and the current Mako [37], [38] and HyTES [39] sensors. The MAGI design concept is therefore easily extendable to Earth orbit [34], where it would provide an option for enhanced performance TIR imaging capability for future missions beyond Landsat 8 and HypsIRI.

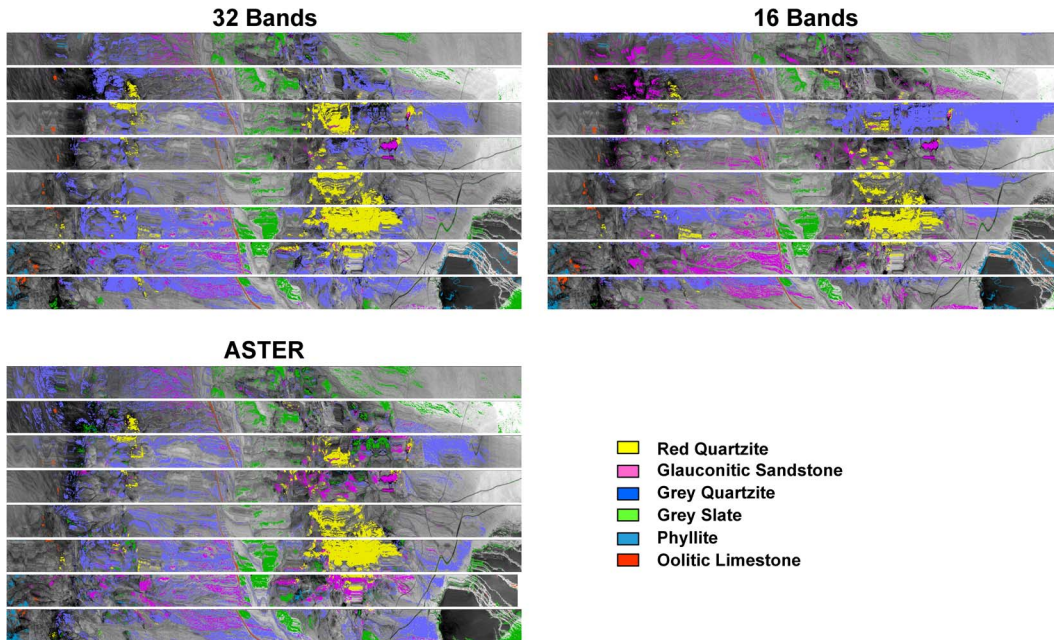


Fig. 5. Computed mineralogy of Cuprite as a function of the number of spectral bands using SEBASS TIR data. Each horizontal strip represents a separate flight line [34].

A dispersive spectrometer architecture was selected because the attendant photon efficiency advantages are more conducive to the faster frame-rate needs of the wide-swath moderate spectral resolution applications that MAGI is intended to address [40], [41]. The specific configuration chosen for the spectrometer is the Dyson design because it provides a compact volume with low optical distortions (smile and keystone, each $< 5\%$ of the pixel pitch) and excellent image quality, even at low f-number. Our design modifies the original Dyson concept by adding an aspherical “corrector” plate [42], [43], which results in a more practical design that allows the object and image planes to be moved away from the surface of the Dyson lens (see Fig. 6). The optically faster design translates into a smaller spectrometer, with a much lower optical bench cooling power requirement, and shorter pixel integration times. Both of these permit larger areal coverage scanning, which is crucial for minimizing revisit times of future orbital sensors. The spherical concave grating at the heart of the spectrometer requires a relatively coarse pitch of ~ 3 grooves/mm. The general principles underlying the MAGI Dyson spectrometer design are described in further detail elsewhere [44]. The MAGI spectrometer was manufactured by Corning Specialty Materials to Aerospace Corporation specifications.

MAGI is descended from a lineage of airborne TIR imagers that use extrinsic Si:As blocked-impurity-band detector arrays [20], [37]. However, the operating temperature for these arrays (10 K) is beyond the current state of the art of mechanical cryocooler technology in a reasonably sized package. Therefore, in order to preclude the need for liquid cryogenics and thereby preserve the space traceability option for MAGI, system considerations favored using HgCdTe for the focal plane array (FPA). The FPA selected was a model TCM-1140 128×128 array manufactured by Rockwell International (now Teledyne) with $40\text{-}\mu\text{m}$ square pixels and ~ 0.8 quantum efficiency across the MAGI spectral range. This array is capable of frame rates up

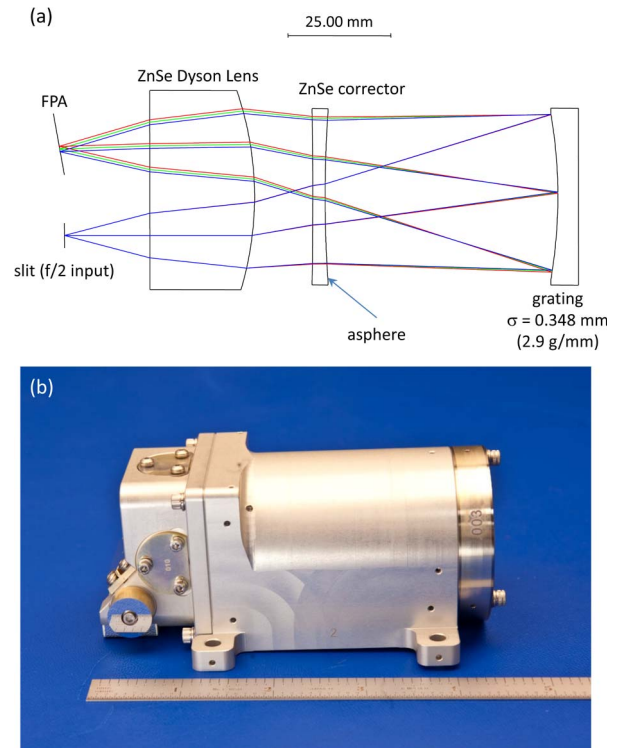


Fig. 6. MAGI Dyson spectrometer. (a) Optical prescription. The slit is normal to the page. (b) Fully assembled: The spectrometer weighs just under 0.5 kg and measures 11.5 cm in length.

to 15 kHz with well depths of up to 27×10^6 electrons and has a long-wavelength cutoff of $14 \mu\text{m}$. The readout integrated circuit is a direct-injection cell design with 32 output taps, each handling $4 \text{ pixels} \times 128 \text{ pixels}$. In the MAGI sensor design, only eight of these taps are used because there are only 32 rows in the spectral dimension. The 128 pixels in the other dimension comprise the spatial extent of the sensor.

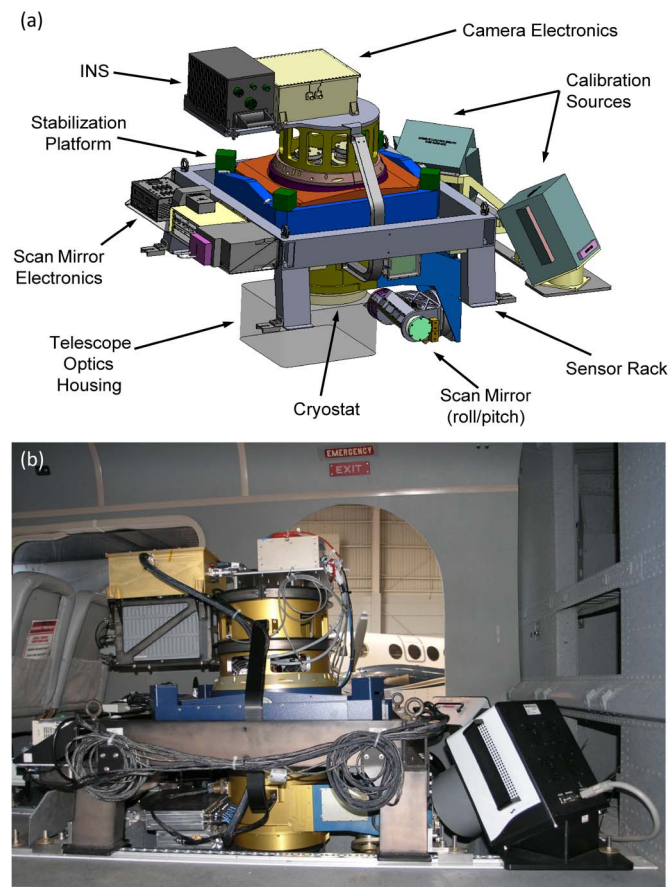


Fig. 7. MAGI instrument. (a) CAD model. (b) Completed instrument installed in a DeHavilland DHC-6 Twin Otter aircraft.

The completed sensor is depicted in Fig. 7. A section cooled to cryogenic temperatures comprises focal imaging optics, slit, dispersive spectrometer subassembly, and FPA. A blocking filter and cold stop near the cryostat window facilitate thermal management and limit out-of-field background radiation flux into the spectrometer. The cryogenic section was configured to be independently operable to facilitate laboratory testing. Cooling is accomplished by two Stirling free-piston cryocoolers (one each for the FPA and the spectrometer) manufactured by Sunpower, Inc. These are connected to the sensor via high-thermal-conductance flexible links manufactured by the Space Dynamics Laboratory of Utah State University, Logan, UT, USA.

An afocal external telescope reduces the instantaneous field-of-view (IFOV) of the cryogenic optics and also relays the cold pupil from inside the cryogenic section to a real (as opposed to virtual) accessible external location in order to minimize the size of the sensor pointing mirror and blackbody calibrators, which are located near the external pupil. The afocal interface between the external telescope and the cryogenic optics reduces the sensitivity of the system to axial (defocus) and lateral misalignment across the warm/cold interface. The overall sensor architecture is modular in design, which is a particularly important feature with regard to the fore optics, which can be readily exchanged in order to adjust the IFOV according to the needs of different platforms flying at a variety of altitudes. The sensor

TABLE I
MAGI PERFORMANCE PARAMETERS

Parameter	Specification
Spectral channels	32
Wavelength coverage	7.1 – 12.7 μm
Instantaneous pixel FOV	0.53 mrad
Frame rate	955 Hz
Integration time	280 μs
Noise-equivalent temp. difference (single frame)	~ 0.13 K at 10 μm
Along-track pixels	128
Maximum cross-track scan angle	$\pm 42^\circ$ (2800 pixels)
Maximum cross-track scans	Unlimited
Detector	HgCdTe
Detector temperature	55 K
Optics temperature	120 K
Calibration	Full-aperture blackbody

can be also operated as a focal system independently of an external telescope, which is a convenience for laboratory testing.

MAGI utilizes a whiskbroom scanning geometry that generates a scene image by sequentially accumulating cross-track scans, or “whisks,” perpendicular to the aircraft flight track. In this scheme, the sensor’s 128-pixel linear field-of-view (FOV) is continuously scanned normal to the direction of travel to generate each whisk, with each whisk comprising up to 2800 frames (the precise frame number being user programmable), thereby producing a 2800 pixel \times 128 pixel image. The scan mirror scans one pixel IFOV during the FPA frame time. Each spatial pixel comprises a spectrum with 32 spectral channels. This approach permits areal coverage rates of up to 20 km²/min at 2-m GSD.

IV. SENSOR PERFORMANCE

The performance parameters of MAGI are summarized in Table I. The performance measurements determine how well the aligned spectrometer matches the optical predictions and also determines the spectral noise behavior. The measurements also determine wavelength smile (change in wavelength of a spectral channel as a function of spatial pixel number), keystone distortion (change in spatial pixel as a function of wavelength for a point source at infinity), and stray light susceptibility (erroneous signals caused by out-of-field sources).

A. Wavelength Grid and Smile Measurement

The calibration process implemented determines the center wavelengths of every pixel in the array. The wavelength smile across the array may be determined from the fitted wavelength grid. The data required to determine this grid are separate images of both hot and cold (ambient temperature) blackbody targets, both with and without wavelength calibration films in front. The calibration films are made of various thin plastics and are NIST-certified and calibrated for transmission and absolute wavelength. They are slightly roughened to minimize interference fringes and are characterized at high spectral resolution. The measured MAGI data are processed to transmission for every pixel as follows:

$$\tau = \frac{HF - CF}{H - C} \quad (1)$$

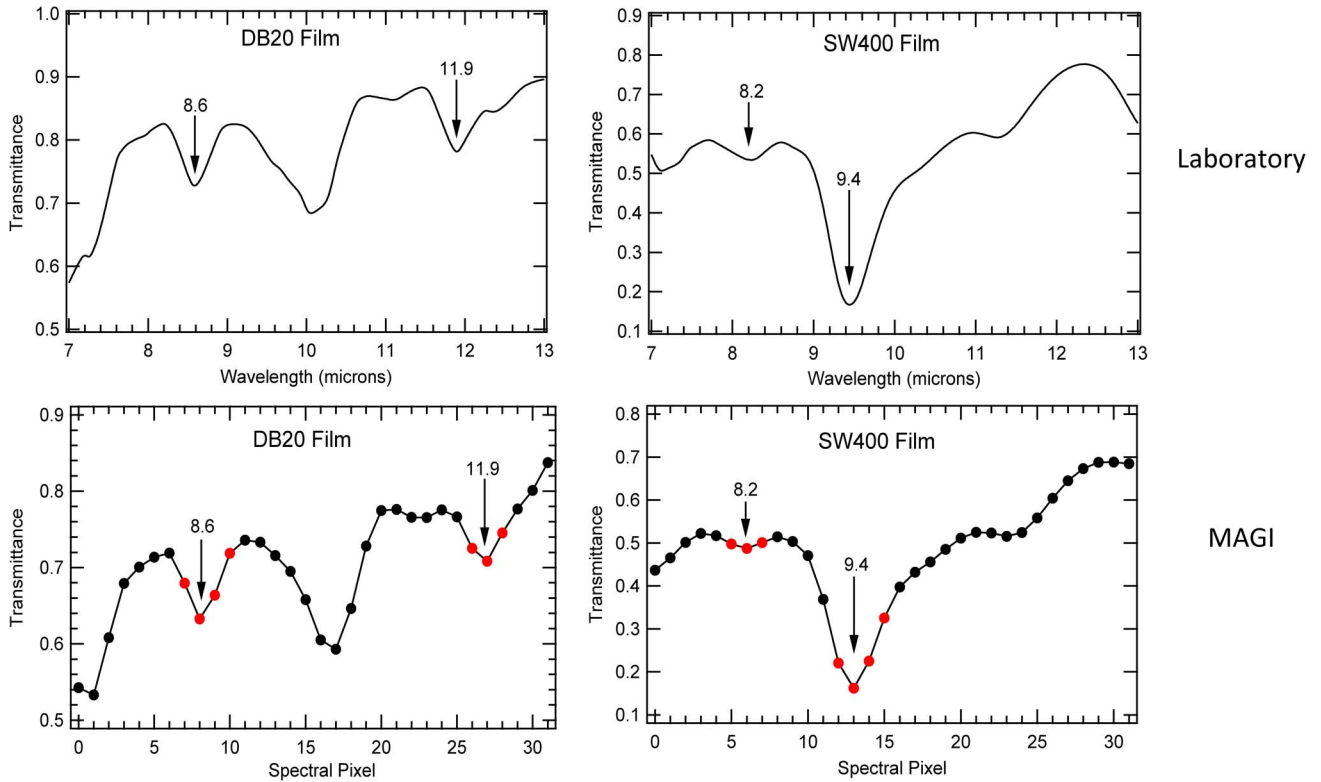


Fig. 8. Laboratory transmission spectra, resampled to MAGI resolution, of the two NIST-certified calibration films used for wavelength determination, and two examples of measured MAGI spectra. The four absorption features, two per film, and their center wavelengths are indicated by arrows. The MAGI wavelength channels that are used in the calibration process are denoted in red.

where

- HF hot blackbody radiance viewed through calibration film;
- CF cold blackbody radiance viewed through calibration film;
- H hot blackbody radiance;
- C cold blackbody radiance.

For the MAGI calibration, two different films are used to provide sharp spectral features spread throughout the spectral bandpass. Fig. 8 shows the laboratory transmission spectra of the two films used, resampled to MAGI spectral resolution, and two examples of measured MAGI spectra. For ease of computation, the spectral resolution function for MAGI is modeled as triangular, with maximum intensity at the center of the pixel and falling to zero at the centers of the adjacent spectral pixels, as predicted by the optical ray trace. Thus, the spectral response function full width at half maximum is 1.0 pixel.

The fitting procedure proceeds in two stages. In the first stage, for each spatial line of the focal plane, the transmission values for the pixels that fall on each of the four absorption features (two features per plastic film) are saved, and a non-linear least square fitting procedure is run separately for each of the calibration film absorption peaks. The procedure uses three adjustable parameters to best fit the laboratory spectrum of each peak: the wavelength of one of the channels near the peak absorption (wavelengths of the other channels are constrained to be an integral number of channel spacings apart); a transmission offset; and a transmission scaling parameter.

The results of the first fitting procedure are input into a second least square fit, which is linear in the fit coefficients. This procedure uses the array of wavelengths from the four fitted absorption peaks for every spatial row. The wavelength data are fit to a wavelength grid of the form

$$\lambda = a_0 + a_1y + a_2x + a_3xy \tag{2}$$

where x is the spatial row number and y is the spectral row number. Coefficient a_0 is the starting wavelength for the array (spatial row 0), and a_1 is the wavelength dispersion between spectral pixels. In general, coefficients a_{0-3} slightly change each time the instrument is thermally cycled. The measured value for the dispersion was within 0.06% of the target value, indicating that accommodation measures implemented to account for the effects of cold optics (dimensional and refractive index changes) were optimal.

Because of the “smile” wavelength distortion, the spectra of different spatial points in the FOV are not measured at exactly the same wavelengths. This small wavelength shift across the FOV complicates data analysis. To overcome this difficulty, radiance values at each pixel are interpolated using a 1-D cubic fitting procedure to a single wavelength grid.

B. Stray Light Measurement

Quantitative testing of stray light performance was carried out by moving a hot point source (a hot soldering iron placed behind an iris) across the narrow dimension of the slit image

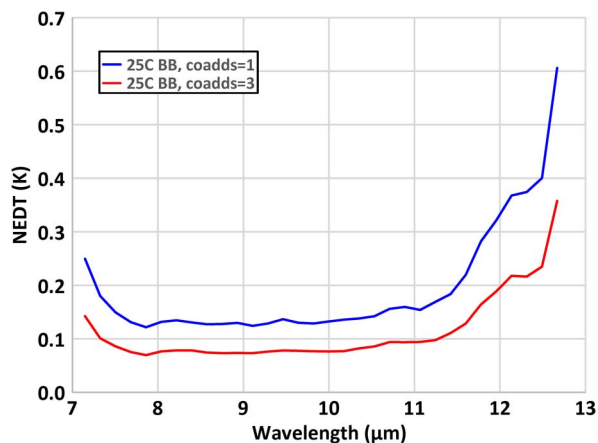


Fig. 9. Sensor NEDT for one and three coadded frames and a frame integration time of 280 μs . The curves represent the median value over all spatial rows.

in the far field. This measurement was completed at a single position along the long dimension of the slit. The acquisition conditions were such that there was a $\sim 300:1$ signal-to-noise ratio (SNR) when the point source was centered on the slit compared with the noise on the background when it was far away from the slit. These measurements indicated that stray light contributions do not exceed 0.3% of the peak intensity.

C. Keystone Distortion

The stray light data may be also used to determine the keystone distortion for the MAGI spectrometer by fitting the measured intensity distributions to a Gaussian profile with a nonlinear least square procedure to extract the peak center position and width. This procedure showed that the center positions for three different wavelengths spanning the instrumental bandpass (i.e., 8.2, 10.2, and 11.4 μm) are coincident to < 0.01 pixel and the $1/e$ widths to within $\pm 2\%$.

D. Sensor Noise Performance

The sensor noise-equivalent temperature difference (NEDT) is assessed by computing the standard deviation of the frame-to-frame noise while the sensor views a blackbody calibration source. Typically, a data set consisting of 100 sequential frames of a blackbody target is used to compute the single-frame NEDT. Fig. 9 shows the measured NEDT for two different instances of frame coadding. The curves are essentially unchanged when viewing either a hot (308 K) or a cold (298 K) blackbody, indicating that the sensor is not background limited, which is attributable to the dominance of electronic readout noise. To maximize the swath width, the sensor does not coadd frames, but for higher sensitivity work, the scan mirror rate can be slowed so that consecutive frames can be coadded, resulting in a smaller swath width.

V. SAMPLE IMAGERY

The inaugural MAGI flight trials were conducted in December 2011, and the sensor performed nominally during these flights. Four primary targets were chosen based on the

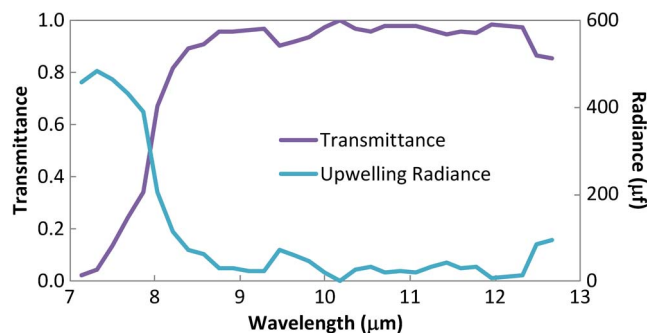


Fig. 10. Atmospheric compensation spectra computed using the ISAC method from data acquired over Salton Sea, CA, on December 9, 2011, from an altitude of 3 km above ground level (AGL).

desire to give a representative sample of geologic, urban, and agriculture environments. These included overflights of the Salton Sea and Coso geothermal fields in California; Cuprite, Nevada; the California Central Valley agricultural region; and several urban locations within the Los Angeles Basin. The sensor was installed in a DeHavilland Twin Otter aircraft and flown over these targets at altitudes up to 3.8 km above mean sea level. For the purposes of this paper, only one of these locations (Salton Sea, CA) is discussed. MAGI data from other sites will be treated in a follow-up science-focused paper currently in preparation.

Validation of the airborne data proceeded in three stages: determination of the optimum data calibration methods, atmospheric compensation of the data, and demonstration of retrieval results for selected data sets. A procedure for identifying and compensating for inoperative and poorly performing pixels (both excessively noisy ones and so-called “blinkers”, i.e., those exhibiting sporadic large signal excursions) was also implemented.

Radiometric calibration is accomplished using two high-emissivity blackbody calibration sources that overfill the sensor FOV and are operated at different known temperatures. One of these sources is controlled to a temperature representative of the coldest targets in the scene, and the other is regulated at a temperature slightly higher than the expected maximum scene temperature. The FPA has very linear response over the typical radiance range exhibited by ground targets so that two-point (gain and offset) calibration is valid. Typically, calibration sets are recorded both before and after each acquisition flight line. FPA drift considerations meant that, for adequate calibration, a given flight line was restricted to no more than 150 whisks. A sensor NESR curve is also computed from these data.

A. Atmospheric Compensation

Atmospheric compensation of the data was accomplished using the ISAC procedure [29] adapted to the spectral resolution of MAGI. The downwelling radiance term is ignored due to its negligible contribution because of the cold temperature and low water vapor content of the atmosphere for these data, as well as the relatively high emissivity of many of the surfaces. An example of the retrieved atmospheric compensation spectra is shown in Fig. 10. The major effect of the compensation is at the

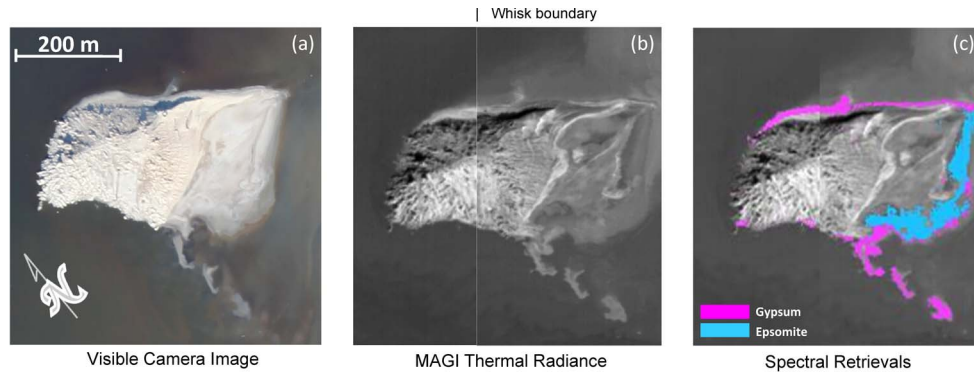


Fig. 11. Airborne image of Mullet Island, Salton Sea, CA, acquired at 3 km AGL. (a) True-color visible image acquired by a boresighted DSLR camera. (b) MAGI 10- μm thermal radiance image. (c) Spectral detection indicating the presence of evaporite minerals. Ground sample distance is 1.6 m.

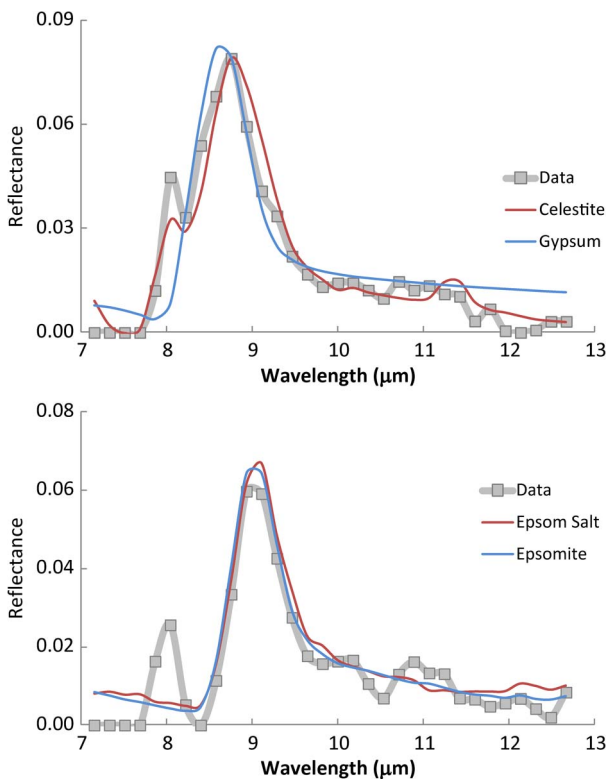


Fig. 12. Two retrieved TIR spectra from the MAGI Mullet Island data converted to reflectance. For each MAGI spectrum, the two best-fitting ASTER library spectra are shown. Note the discrimination of the small spectral feature at $\sim 8.0 \mu\text{m}$ and the difference in wavelength position of the primary absorption feature at $\sim 8.8 \mu\text{m}$ in the top panel, which attest to the need for the spectral resolution of MAGI.

shorter wavelengths at the edge of the atmospheric transmission window.

B. Salton Sea Mineral Identification

MAGI data were acquired over Mullet Island and the active geothermal features ($33^{\circ}13'31''$ N; $115^{\circ}36'30''$ W) in the SE portion of the hypersaline endorheic Salton Sea (Imperial County, CA). These data were analyzed for surface spectral features by comparing against library spectra from the ASTER database [45]. Concurrent thermal and visible imagery of the

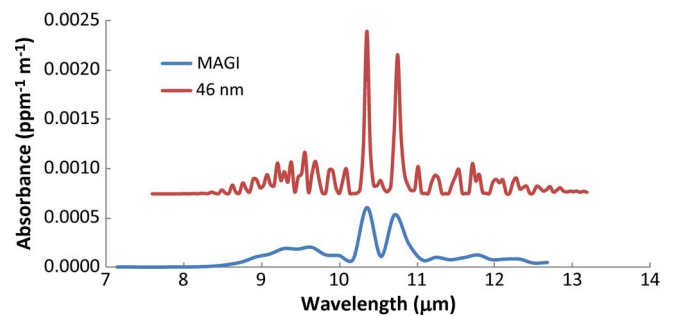


Fig. 13. TIR absorption spectra of ammonia at 46-nm resolution and resampled to the resolution of MAGI (175 nm). The higher resolution spectrum is vertically offset for clarity.

island are shown in Fig. 11, whereas Fig. 12 shows the best two matches for four characteristic spectra indicating the predominant mineralogy. The main body of the island is encrusted with bird guano and therefore does not match any of the expected lithotypes (Robinson *et al.* [46] report that the island is volcanic with various stages of hydrothermal alteration); however, the low-lying wave-washed fringes of the island do yield spectral signatures corresponding to evaporite deposits commonly associated with highly mineralized evaporative water bodies such as Salton Sea [47], [48].

C. Detection of Ammonia from a Geothermal Vent

In the same flight line as Mullet Island, a cluster of active geothermal vents [49] was imaged close to the southeast shoreline of Salton Sea. These vents emit ammonia, which had previously been detected by other sensors in recent years [22]. The narrow diagnostic spectral features of ammonia provide a stringent test of the MAGI spectral resolution paradigm. The earlier ammonia detections from this site were carried out with the 46-nm (128-channel) resolution SEBASS instrument. Although the reduced spectral resolution of MAGI tends to suppress the diagnostic TIR ammonia features (see Fig. 13), a plume of ammonia was nevertheless detected near the center of the fumarole field with an SNR of ~ 3 (Fig. 14), attesting to the high radiometric sensitivity of the MAGI sensor. This retrieval was achieved despite a low-temperature contrast ΔT between the surface and ambient air, which reduces the measurement

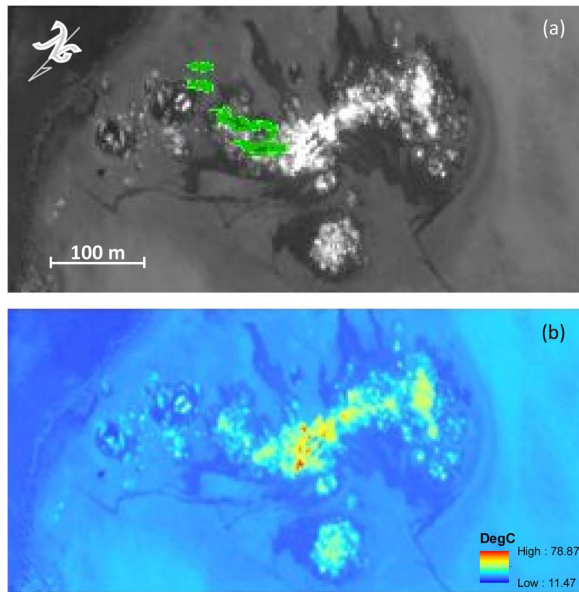


Fig. 14. (a) 10- μm radiance image of geothermal vents near the SE edge of Salton Sea, CA. Detected ammonia emissions are superimposed in green with depth of hue indicating signal strength. (b) Corresponding brightness temperature map. Sensor altitude is 3 km AGL. Ground sample distance is 1.6 m.

sensitivity. In this instance, ΔT was estimated to be only ~ 2 K, which is considerably lower than the 10–20 K values prevailing for the prior data collections where ammonia emission was observed at the same location but during the spring and summer months [22].

VI. CONCLUSION

An advanced TIR spectral imaging sensor has been built and commissioned to address measurement requirements in support of NASA Earth science goals, as articulated in the National Research Council's Earth Science Decadal Survey report [50]. The procedure employed to derive the desired performance specifications is explained, and the end results are validated by data collected during the inaugural field trials of the completed instrument.

MAGI is a wide-swath moderate spectral resolution imaging spectrometer that spans the 7.1- to 12.7- μm TIR region in 32 contiguous channels. The modified Dyson design allows for a novel compact spectrometer with low cooling power requirements. The spectral resolution was chosen based on the results of several trade studies and represents a balance between accurate mineral/gas detection, precise temperature retrievals, and the extensive power and data requirements of hyperspectral sensors (particularly problematic for orbital instruments). The underlying MAGI design philosophy was validated through an extensive field study involving surrogate data [51], [52] and will be further examined in a paper dedicated to the MAGI data that is currently in preparation. Initial analysis of the MAGI TIR data clearly discriminates surface minerals, greatly expands gas-detection capability, and more accurately retrieves land-surface temperatures relative to the capabilities of current multispectral TIR sensors.

REFERENCES

- [1] "NASA 2008 HypsIRI whitepaper and workshop report," HypsIRI Science Steering Group, Pasadena, CA, USA, JPL Publication 09-19, May 2009. [Online]. Available: https://hypsiri.jpl.nasa.gov/downloads/2008_Workshop/2008%20HypsIRI%20Whitepaper%20and%20Science%20Workshop%20Report-r2.pdf
- [2] M. S. Ramsey, V. J. Realmuto, G. C. Hulley, and S. J. Hook, "HypsIRI thermal infrared (TIR) band study report," Jet Propulsion Lab., Pasadena, CA, USA JPL Publication 12-16, Oct. 2012. [Online]. Available: hypsiri.jpl.nasa.gov/downloads/reports_whitepapers/HypsIRI_TIR_Band_Report_gchv1_VJRv1_pmbv1_MSRv2_1.pdf
- [3] M. S. Ramsey and L. P. Flynn, "Strategies, insights, and the recent advances in volcanic monitoring and mapping with data from NASA's Earth Observing System," *J. Volcanol. Geothermal Res.*, vol. 135, no. 1/2, pp. 1–11, Jul. 2004.
- [4] M. Ramsey and J. Dehn, "Spaceborne observations of the 2000 Bezymianny, Kamchatka eruption: The integration of high-resolution ASTER data into near real-time monitoring using AVHRR," *J. Volcanol. Geothermal Res.*, vol. 135, no. 1/2, pp. 127–146, Jul. 2004.
- [5] H. E. Thomas and I. M. Watson, "Observations of volcanic emissions from space: Current and future perspectives," *Natural Hazards*, vol. 54, no. 2, pp. 323–354, Oct. 2009.
- [6] J. A. Sobrino, M. Gomez, J. C. Jimenez-Munoz, and A. Olioso, "Application of a simple algorithm to estimate daily evapotranspiration from NOAA-AVHRR images for the Iberian Peninsula," *Remote Sens. Environ.*, vol. 110, no. 2, pp. 139–148, Sep. 2007.
- [7] A. N. French *et al.*, "Detecting land cover change at the Jornada Experimental Range, New Mexico with ASTER emissivities," *Remote Sens. Environ.*, vol. 112, no. 4, pp. 1730–1748, Apr. 2008.
- [8] M. C. Anderson, C. R. Hain, B. Wardlow, J. R. Mecikalski, and W. P. Kustas, "Evaluation of a drought index based on thermal remote sensing of evapotranspiration over the continental U.S.," *J. Clim.*, vol. 24, no. 8, pp. 2025–2044, Apr. 2011.
- [9] D. A. Quattrochi and J. C. Luval, "Thermal infrared remote sensing for analysis of landscape ecological processes: Methods and applications," *Landscape Ecol.*, vol. 14, no. 6, pp. 577–598, Dec. 1999.
- [10] D. A. Roberts, D. A. Quattrochi, G. C. Hulley, S. J. Hook, and R. O. Green, "Synergies between VSWIR and TIR data for the urban environment: An evaluation of the potential for the Hyperspectral Infrared Imager (HypsIRI) Decadal Survey mission," *Remote Sens. Environ.*, vol. 117, pp. 83–101, Feb. 2012.
- [11] Y. Yamaguchi, A. B. Kahle, H. Tsu, T. Kawakami, and M. Pniel, "Overview of Advanced Spaceborne Thermal Emission and Reflection Radiometer (ASTER)," *IEEE Trans. Geosci. Remote Sens.*, vol. 36, no. 4, pp. 1062–1071, Jul. 1998.
- [12] Y. Ninomiya, "Mapping quartz, carbonate minerals and mafic-ultramafic rocks using remotely sensed multispectral thermal infrared ASTER data," in *Proc. SPIE*, Mar. 2002, vol. 4710, pp. 191–202.
- [13] L. C. Rowan, J. C. Mars, and C. J. Simpson, "Lithologic mapping of the Mordor, NT, Australia ultramafic complex by using the Advanced Spaceborne Thermal Emission and Reflection Radiometer (ASTER)," *Remote Sens. Environ.*, vol. 99, no. 1/2, pp. 105–126, Nov. 2005.
- [14] R. D. Hewson, T. J. Cudahy, S. Mizuhiko, K. Ueda, and A. J. Mauger, "Seamless geological map generation using ASTER in the Broken Hill-Curnamona province of Australia," *Remote Sens. Environ.*, vol. 99, no. 1/2, pp. 159–172, Nov. 2005.
- [15] P. R. Christensen *et al.*, "Thermal emission spectrometer experiment: Mars Observer mission," *J. Geophys. Res.*, vol. 97, no. E5, pp. 7719–7734, May 1992.
- [16] P. R. Christensen *et al.*, "Initial results from the Mini-TES experiment in Gusev Crater from the Spirit Rover," *Science*, vol. 305, no. 5685, pp. 837–842, Aug. 2004.
- [17] A. Barducci *et al.*, "Emissivity and temperature assessment using a maximum entropy estimator: Structure and performance of the MaxEnTES algorithm," *IEEE Trans. Geosci. Remote Sens.*, vol. 53, no. 2, pp. 738–751, Feb. 2014.
- [18] A. N. French *et al.*, "Surface energy fluxes with the Advanced Spaceborne Thermal Emission and Reflection radiometer (ASTER) at the Iowa 2002 SMACEX site (USA)," *Remote Sens. Environ.*, vol. 99, no. 1/2, pp. 55–65, Nov. 2005.
- [19] S. Scheidt, M. S. Ramsey, and N. Lancaster, "Determining soil moisture and sediment availability at White Sands Dune Field, NM from apparent thermal inertia (ATI) data," *J. Geophys. Res.*, vol. 115, no. F2, Jun. 1–23, 2010, Art. ID. F02019.
- [20] J. A. Hackwell *et al.*, "LWIR/MWIR imaging hyperspectral sensor for airborne and ground-based remote sensing," in *Proc. SPIE*, Nov. 1996, vol. 2819, pp. 102–107.

- [21] S. J. Young, "Detection and quantification of gases in industrial-stack plumes using thermal infrared hyperspectral imaging," *Aerosp. Corp.*, El Segundo, CA, USA, *Aerosp. Rep. No. ATR-2002(8407)-1*, Feb. 2002.
- [22] D. M. Tratt *et al.*, "Remotely sensed ammonia emission from fumarolic vents associated with a hydrothermally active fault in the Salton Sea Geothermal Field, California," *J. Geophys. Res.*, vol. 116, no. D21, Nov. 1–10, 2011, Art. ID. D21308.
- [23] S. W. Sharpe *et al.*, "Gas-phase databases for quantitative infrared spectroscopy," *Appl. Spectrosc.*, vol. 58, no. 12, pp. 1452–1461, Dec. 2004.
- [24] P. L. Hanst and S. T. Hanst, "Infrared spectra for quantitative analysis of gases," *Infrared Analysis, Inc.*, Anaheim, CA, USA, 1993.
- [25] L. S. Rothman *et al.*, "The HITRAN molecular spectroscopic database and HAWKS (HITRAN Atmospheric Workstation): 1996 Edition," *J. Quant. Spectrosc. Radiat. Transfer*, vol. 60, no. 5, pp. 665–710, Nov. 1998.
- [26] R. G. Resmini, M. E. Kappus, W. S. Aldrich, J. C. Harsanyi, and M. Anderson, "Mineral mapping with HYperspectral Digital Imagery Collection Experiment (HYDICE) sensor data at Cuprite, Nevada, USA," *Int. J. Remote Sens.*, vol. 18, no. 7, pp. 1553–1570, Jul. 1997.
- [27] F. A. Kruse, "Combined SWIR and LWIR mineral mapping using MASTER/ASTER," in *Proc. IEEE IGARSS*, 2002, vol. 4, pp. 2267–2269.
- [28] D. N. Riley and C. A. Hecker, "Mineral mapping with airborne hyperspectral thermal infrared remote sensing at Cuprite, Nevada, USA," in *Thermal Infrared Remote Sensing, Remote Sens. Digital Image Processing*. Dordrecht, Netherlands: Springer-Verlag, May 2013, vol. 17, pp. 495–514.
- [29] S. J. Young, B. R. Johnson, and J. A. Hackwell, "An in-scene method for atmospheric compensation of thermal hyperspectral data," *J. Geophys. Res.*, vol. 107, no. D24, p. ACH14, Dec. 1–20, 2002.
- [30] M. E. Winter, "N-FINDR: An algorithm for fast autonomous spectral end-member determination in hyperspectral data," in *Proc. SPIE*, Oct. 1999, vol. 3753, pp. 266–275.
- [31] M. Abrams, "ASTER: Advanced spaceborne thermal emission and reflection radiometer," U.S. Geol. Survey, Reston, VA, USA, Aug. 2005. [Online]. Available: asterweb.jpl.nasa.gov/aster_talk.zip
- [32] P. R. Christensen *et al.*, "Mars Global Surveyor Thermal Emission Spectrometer experiment: Investigation description and surface science results," *J. Geophys. Res.*, vol. 106, no. E10, pp. 23823–23872, Oct. 2001.
- [33] P. R. Christensen *et al.*, "Miniature thermal emission spectrometer for the Mars exploration rovers," *J. Geophys. Res.*, vol. 108, no. E12, p. 8064, Dec. 1–23, 2003.
- [34] J. L. Hall, J. A. Hackwell, D. M. Tratt, D. W. Warren, and S. J. Young, "Space-based mineral and gas identification using a high-performance thermal infrared imaging spectrometer," in *Proc. SPIE*, Sep. 1–9, 2008, vol. 7082, Art. ID. 70820M.
- [35] S. J. Hook, J. J. Myers, K. J. Thome, M. Fitzgerald, and A. B. Kahle, "The MODIS/ASTER airborne simulator (MASTER)—A new instrument for earth science studies," *Remote Sens. Environ.*, vol. 76, no. 1, pp. 93–102, Apr. 2001.
- [36] T. A. Ellis *et al.*, "The NASA enhanced MODIS airborne simulator," in *Proc. SPIE*, Sep. 1–9, 2011, vol. 8153, Art. ID. 81530N.
- [37] D. W. Warren, R. H. Boucher, D. J. Gutierrez, E. R. Keim, and M. G. Sivjee, "MAKO: A high-performance, airborne imaging spectrometer for the long-wave infrared," in *Proc. SPIE*, Aug. 1–10, 2010, vol. 7812, Art. ID. 78120N.
- [38] J. L. Hall *et al.*, "First flights of a new airborne thermal infrared imaging spectrometer with high area coverage," in *Proc. SPIE*, May 1–7, 2011, vol. 8012, Art. ID. 801203.
- [39] S. J. Hook, W. R. Johnson, and M. J. Abrams, "NASA's Hyperspectral Thermal Emission Spectrometer (HyTES)," *Remote Sens. Digit. Image Process.*, vol. 17, pp. 93–115, May 2013.
- [40] M. T. Eismann, C. R. Schwartz, J. N. Cederquist, J. A. Hackwell, and R. J. Huppi, "Comparison of infrared imaging hyperspectral sensors for military target detection applications," in *Proc. SPIE*, Nov. 1996, vol. 2819, pp. 91–101.
- [41] L. W. Schumann and T. S. Lomheim, "Infrared hyperspectral imaging Fourier transform and dispersive spectrometers: Comparison of signal-to-noise-based performance," in *Proc. SPIE*, Jan. 2002, vol. 4480, pp. 1–14.
- [42] D. W. Warren, D. J. Gutierrez, and E. R. Keim, "Dyson spectrometers for high-performance infrared applications," *Opt. Eng.*, vol. 47, no. 10, Oct. 1–9, 2008, Art. ID. 103601.
- [43] D. W. Warren, "Compact, high-throughput spectrometer apparatus for hyperspectral remote sensing," U.S. Patent 7 609 381, Sep. 24, 2009. [Online]. Available: www.google.com/patents/US20090237657
- [44] D. W. Warren, D. J. Gutierrez, J. L. Hall, and E. R. Keim, "Dyson spectrometers for infrared earth remote sensing," in *Proc. SPIE*, Sep. 1–8, 2008, vol. 7082, Art. ID. 70820R.
- [45] A. M. Baldridge, S. J. Hook, C. I. Grove, and G. Rivera, "The ASTER spectral library version 2.0," *Remote Sens. Environ.*, vol. 113, no. 4, pp. 711–715, Apr. 2009.
- [46] P. T. Robinson, W. A. Elders, and L. J. P. Muffler, "Quaternary volcanism in the Salton Sea geothermal field, Imperial Valley, California," *Geol. Soc. Amer. Bull.*, vol. 87, no. 3, pp. 347–360, Mar. 1976.
- [47] R. J. Spencer, "Sulfate minerals in evaporite deposits," *Rev. Mineralogy Geochem.*, vol. 40, no. 1, pp. 173–192, Jan. 2000.
- [48] M. A. Tiffany, S. L. Ustin, and S. H. Hurlbert, "Sulfide eruptions and gypsum blooms in the Salton Sea as detected by satellite imagery, 1979–2006," *Lake Reservoir Manage.*, vol. 23, no. 5, pp. 637–652, Dec. 2007.
- [49] D. K. Lynch, K. W. Hudnut, and P. M. Adams, "Development and growth of recently-exposed fumarole fields near Mullet Island, Imperial County, California," *Geomorphology*, vol. 195, pp. 27–44, Aug. 2013.
- [50] NRC, Committee on Earth Science and Applications from Space, *Earth Science and Applications from Space: National Imperatives for the Next Decade and Beyond*. Washington, DC, USA: National Academies Press, 2007. [Online]. Available: www.nap.edu/catalog/11820.html
- [51] K. A. Reath and M. S. Ramsey, "Exploration of geothermal systems using hyperspectral thermal infrared remote sensing," *J. Volcanol. Geothermal Res.*, vol. 265, pp. 27–38, Sep. 2013.
- [52] K. A. Reath, "Hyperspectral thermal infrared analysis of the Salton sea geothermal field," M.S. thesis, Univ. Pittsburgh, Pittsburgh, PA, USA, Sep. 2011. [Online]. Available: d-scholarship.pitt.edu/9188



Jeffrey L. Hall received the Ph.D. degree in physical chemistry from Rice University, Houston, TX, USA, in 1986.

In late 1986, he joined The Aerospace Corporation, Los Angeles, CA, USA, where he is currently a Senior Scientist with the Space Science Applications Laboratory. He has been the Principal Investigator for the development of several hyperspectral imaging sensors, including sensors for unmanned aerial vehicles and unattended ground sensors. He has a particular interest in performance modeling of these instruments, radiative transfer modeling, and the development of automated target detection algorithms. His research interests are in the area of infrared hyperspectral imaging from both ground-based and airborne platforms.

Richard H. Boucher, photograph and biography not available at the time of publication.

Kerry N. Buckland, photograph and biography not available at the time of publication.

David J. Gutierrez, photograph and biography not available at the time of publication.

John A. Hackwell, photograph and biography not available at the time of publication.

B. Robert Johnson, photograph and biography not available at the time of publication.

Eric R. Keim, photograph and biography not available at the time of publication.

Nery M. Moreno, photograph and biography not available at the time of publication.



Michael S. Ramsey received the B.S. degree in mechanical engineering from Drexel University, Philadelphia, PA, USA, in 1990 and the Ph.D. degree in geology from Arizona State University, Tempe, AZ, USA, in 1996.

He is currently a Professor with the Department of Geology and Planetary Science, University of Pittsburgh, Pittsburgh, PA, where he also manages the Image Visualization and Infrared Spectroscopy Laboratory, which is a state-of-the-art image analysis and infrared spectroscopy facility supported by the National Aeronautics and Space Administration (NASA) and the National Science Foundation. His research interests are quite varied but focus on instrument development, physical volcanology, eolian dynamics, and planetary processes using thermal infrared remote sensing and spectroscopy. He has served as an Appointed Member of the NASA Earth Science Subcommittee and as a Science Team Member on three thermal infrared instruments, namely, the Earth-orbiting Advanced Spaceborne Thermal Emission and Reflectance Radiometer (ASTER), the Mars-orbiting Thermal Emission Imaging System (THEMIS), and the airborne Mineral and Gas Identified (MAGI).

Mazaher G. Sivjee, photograph and biography not available at the time of publication.



David M. Tratt (M'89–SM'97) received the Ph.D. degree from Heriot-Watt University, Edinburgh, U.K., in 1984.

He has specialized in environmental remote sensing for Earth and planetary science applications for more than 25 years. In 1986, he was with the Laser Remote Sensing Group, Jet Propulsion Laboratory, where his research activities involved lidar sensing of the atmosphere. In 2002, he began an assignment at the NASA Earth Science Technology Office (ESTO) to manage a laser technology R&D program targeted toward future space-based Earth science measurement needs. In 2006, he joined The Aerospace Corporation, Los Angeles, CA, USA, where he is currently engaged in the evaluation and development of remote sensing applications for infrared imaging spectrometry in the Earth and planetary sciences.

David W. Warren, photograph and biography not available at the time of publication.

Stephen J. Young, photograph and biography not available at the time of publication.